

# Gadolinium Metallofullerene-Polypyrrole Nanoparticles for Activatable Dual-Modal Imaging-Guided Photothermal Therapy

Sheng Wang,<sup>†,‡</sup> Zijian Zhou,<sup>‡</sup> Guocan Yu,<sup>‡</sup> Nan Lu,<sup>‡</sup> Yijing Liu,<sup>‡</sup> Yunlu Dai,<sup>‡</sup> Xiao Fu,<sup>‡</sup> Jing Wang,<sup>\*,†</sup> and Xiaoyuan Chen<sup>\*,‡</sup>

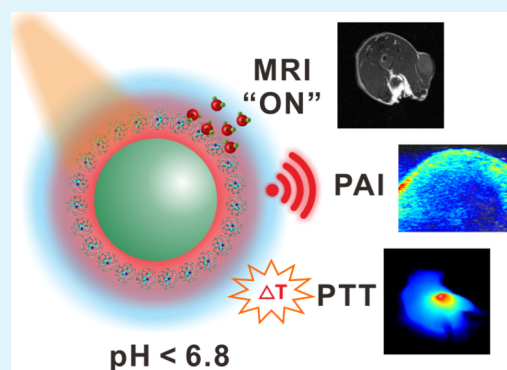
<sup>†</sup>Department of Nuclear Medicine, Xijing Hospital, Fourth Military Medical University, Xi'an 710032, China

<sup>‡</sup>Laboratory of Molecular Imaging and Nanomedicine, National Institute of Biomedical Imaging and Bioengineering, National Institutes of Health, Bethesda, Maryland 20892, United States

## Supporting Information

**ABSTRACT:** Accurate diagnosis of tumor is promising to guide photothermal therapy (PTT) for efficacious tumor ablation with minimal damage to healthy tissues. Here, we report an activatable dual-modal imaging agent, which is based on PEGylated-gadolinium metallofullerene-polypyrrole nanoparticle (PEG-GMF-PPy NP) for imaging-guided PTT. A contrast agent (gadolinium metallofullerene, GMF) with excellent magnetic resonance imaging (MRI) performance and an ultra-pH-responsive polymer (PEG-PC7A) are successively modified to the surface of photothermal agent (PPy NP). The prepared PEG-GMF-PPy NPs show strong absorption in the near-infrared (NIR) region, so they can be utilized for photoacoustic imaging. Furthermore, in a tumor extracellular environment, the PEG-GMF-PPy NPs can achieve pH-enhanced MRI because of the hydrophobic-to-hydrophilic conversion of the PC7A. Upon accurate diagnosis-guided NIR laser irradiation, excellent tumor ablation effect is achieved. The results suggest that the PEG-GMF-PPy NPs are promising agents for activatable imaging-guided PTT.

**KEYWORDS:** activatable contrast agent, photoacoustic imaging, photothermal therapy, gadolinium metallofullerene, polypyrrole



## 1. INTRODUCTION

Photothermal therapy (PTT) is a promising cancer treatment technique because of its effective tumor ablation.<sup>1–6</sup> In the past few years, various near infrared (NIR) light-absorbing photothermal agents (e.g., metallic, transition-metal chalcogenide-based, and carbon-based nanomaterials and organic NIR dyes) have been developed for PTT of tumor.<sup>7–14</sup> Particularly, imaging-guided PTT has been considered as a promising strategy for in vivo applications. Imaging can identify the tumor location and size, and the NIR light can be applied only in the tumor site; thus accurate imaging-guided PTT can achieve improved selectivity and minimal damage to healthy tissues.<sup>15–19</sup>

In order to achieve more accurate tumor diagnosis, various activatable imaging probes that respond to tumor micro-environments have been developed for enhanced tumor imaging.<sup>20–22</sup> Compared to conventional imaging probes, activatable probes can enhance the target-to-background contrast; therefore, the feature of interest is easier to be distinguished.<sup>23,24</sup> Gadolinium metallofullerene (GMF) has been recognized as a potential next-generation contrast agent for magnetic resonance imaging (MRI) because of its high relaxivity.<sup>25–28</sup> Furthermore, the gadolinium (Gd) ions, which may cause associated toxicity, are confined inside fullerene cages, making the GMF safer for in vivo applications when

compared to commercial Gd-chelator agents.<sup>29,30</sup> Although GMFs have been reported for tumor MRI detection, the development of GMF-based activatable MR contrast agents is scant until now.

Considering that each imaging modality suffers its own limitations, another strategy to achieve accurate diagnosis is employing multimodal imaging to furnish complementary information.<sup>31–33</sup> For example, MRI, which has advantages of high spatial resolution and unlimited tissue penetration depth, is a reliable noninvasive imaging modality.<sup>34–36</sup> However, monomodal MRI is difficult to provide sufficient information for accurate diagnosis owing to its limited sensitivity.<sup>37</sup> Photoacoustic imaging (PAI), which detects ultrasound waves produced by contrast agents upon pulsed laser excitation, is a new promising technique with the advantages of both optical imaging and ultrasonic imaging (e.g., high-sensitivity, deep-tissue penetration).<sup>38–43</sup> Therefore, the MRI/PAI dual-modal imaging would conduce to provide more comprehensive imaging features.

Herein, we demonstrate an activatable cancer theranostic agent based on poly(ethylene glycol) (PEG)-GMF-polypyrrole

Received: June 10, 2018

Accepted: August 7, 2018

Published: August 7, 2018

nanoparticles (PEG-GMF-PPy NPs) for dual-modal imaging-guided PTT (Figure 1). In this system, PPy NPs, a kind of

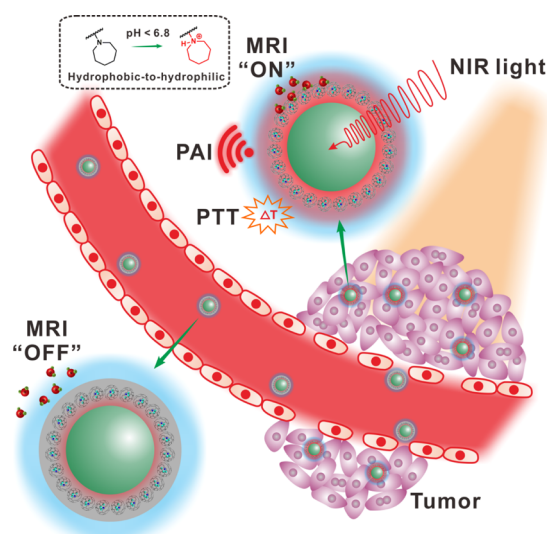


**Figure 1.** Schematic illustration showing the PEG-GMF-PPy NPs for activatable dual-modal imaging-guided PTT.

photothermal conversion agent with high NIR absorbance and significant photothermal stability, were used for PA imaging and PTT. GMF was then absorbed on the PPy NPs through a layer-by-layer method. Then, the GMF-PPy NPs were modified by poly(ethylene glycol)-poly(2-(hexamethyleneimino)ethyl methacrylate)-(methacryloxy)-succinimide (PEG-PC7A-NHS), obtaining PEG-GMF-PPy NPs. At physiological pH (approximately 7.4), the poly(2-(hexamethyleneimino)ethyl methacrylate) (PC7A) chains were hydrophobic; thus, the GMFs were encapsulated into a hydrophobic layer and show low water-exchange efficiency, resulting in relatively low longitudinal relaxivity. However, in the tumor microenvironment ( $pH < 6.8$ ), the protonated hydrophilic PC7A chains allow access of water molecules to the GMF layer, leading to activated MR contrast. Thus, the as-prepared PEG-GMF-PPy NPs can be used for activatable imaging-guided PTT.

## 2. EXPERIMENTAL METHOD

**2.1. Materials.** GMF was purchased from SES Research. mPEG<sub>5k</sub>-NH<sub>2</sub> was purchased from Biochempeg. *N*-(2-Hydroxyethyl)-hexamethyleneimine and polyethyleneimine (PEI, branched,  $M_w$  1200) were purchased from Alfa Aesar. Poly(vinyl alcohol) ( $M_w$  9000–10 000), 4-cyano-4-(phenylcarbonothioylthio)pentanoic acid *N*-succinimidyl ester (RAFT-NHS), methacryloyl chloride, triethylamine, methacrylic acid *N*-hydroxysuccinimide ester (MANHS), 2,2'-azobis(2-methylpropionitrile) (AIBN), ferric chloride, pyrrole, pyrrole-3-carboxylic acid, and methyl thiazolyl tetrazolium (MTT) were obtained from Sigma-Aldrich.

**2.2. Synthesis of PEG-RAFT and PEG-PC7A-NHS.** At first, a PEG-RAFT agent was synthesized by the reaction between PEG-NH<sub>2</sub> and RAFT-NHS (Scheme S1). mPEG-NH<sub>2</sub> (500 mg) and RAFT-NHS (50 mg) were dissolved in dichloromethane (10 mL). After 24 h of reaction, 100 mL of diethyl ether was added to the mixture for precipitation. The precipitate was then dried under vacuum. Then, 2-(hexamethyleneimino)ethyl methacrylate (C7A) monomer was synthesized according to a previous report (Scheme S2).<sup>44</sup> The PEG-PC7A-NHS was synthesized as follows: PEG-RAFT (0.1 mmol), C7A (8 mmol), and AIBN (0.02 mmol) were dissolved in 1,4-dioxane (5 mL) for polymerization (60 °C, 12 h). Then, MANHS (0.3 mmol)

was added into the mixture for another 12 h of polymerization. The product was dialyzed against dimethylformamide and then against pure water. The PEG-PC7A-NHS polymer was collected after freeze-drying.

**2.3. Preparation of PEG-GMF-PPy NPs.** The Gd<sub>3</sub>N@C<sub>80</sub>-NH<sub>2</sub> and PPy NPs were first prepared following reported procedures.<sup>27,45</sup> The PEG-GMF-PPy NPs were prepared through a layer-by-layer method by electrostatic interaction. First, negatively charged PPy NP (5 mg) aqueous solution was added into a PEI (20 mg) solution under sonication. The solution was sonicated and stirred at room temperature and then purified by ultrafiltration (MWCO: 100 kDa), obtaining positively charged P-PPy NPs. Then, the P-PPy solution was added into Gd<sub>3</sub>N@C<sub>80</sub>-NH<sub>2</sub> (1 mg) aqueous solution under sonication. After 2 h of stirring, the solution was purified by centrifugation (10 000 rpm, 15 min). PEG-PC7A-NHS (10 mg) was dissolved in 2-(*N*-morpholino)ethanesulfonic acid buffer solution and added into GMF-PPy NPs aqueous solution. After stirring for 30 min, 1-ethyl-3-(3-(dimethylaminopropyl)-carbodiimide) (5 mg) was added for 6 h of reaction. Thereafter, the solution was dialyzed (MWCO: 100 kDa) against 4-(2-hydroxyethyl)-1-piperazineethanesulfonic acid (pH 7.4) buffer solution to obtain PEG-GMF-PPy NPs.

**2.4. Physicochemical Characterizations of the PEG-GMF-PPy NPs.** The morphologies of the samples were observed by atomic force microscopy and transmission electron microscopy (TEM). The effective particle diameter and zeta potential of the samples were determined by dynamic light-scattering ( $n = 3$ ). Gd concentrations of samples were measured by inductively coupled plasma mass spectrometry (ICP-MS) ( $n = 3$ ). The longitudinal relaxivities of samples were measured using a 7 T MRI system (Bruker, Germany). In vitro PA performance of PEG-GMF-PPy NPs was measured on a Vevo 2100 LAZR system (VisualSonics, Inc., New York).

**2.5. Measurement of the Photothermal Effect.** The aqueous solutions (200  $\mu$ L) of samples were irradiated by a NIR laser (808 nm) for 300 s and their temperature changes were recorded by using a FLIR thermal camera. To determine the photothermal conversion efficiency ( $\eta$ ) of the PPy NPs, the laser was turned on for 300 s and then shut off; the temperature change was recorded in both heating and cooling stages. Then, the  $\eta$  value was calculated following the reported procedure.<sup>33</sup>

**2.6. Cytotoxicity and in Vitro PTT.** U87MG cells (from American type culture collection) were seeded into 96-well plates and treated with different samples for 2 h. Thereafter, 5 min of NIR laser irradiation (1.0 W cm<sup>-2</sup>) was applied to the cells. The cell viabilities were determined by using MTT assay ( $n = 5$ ) and calcein AM/propidium iodide (PI) co-staining assay.

**2.7. In Vivo MRI and PAI.** All animal work was performed under protocols approved by the NIH Animal Care and Use Committee. To prepare U87MG tumor-bearing mice,  $2 \times 10^6$  U87MG cells were subcutaneously injected into the right hind leg of athymic nude mice (Harlan, Indianapolis, IN).

When the tumors reached 80 mm<sup>3</sup>, a total of 100  $\mu$ L (Gd concentration: 50 ppm) of PEG-GMF-PPy NPs solution was intravenously injected into the mice. Then, MRI was performed on a micro-MR scanner (7.0 T, Bruker, Pharmascan) by using a mouse coil. The parameters were as follows: repetition time (TR) = 546.32 ms; echo time (TE) = 9 ms; matrix acquisition =  $256 \times 256$ .

PEG-GMF-PPy NPs solution (5 mg mL<sup>-1</sup>, 100  $\mu$ L) was intravenously injected into U87MG tumor-bearing mice. Then, a Vevo 2100 LAZR system was used to perform PA imaging of tumor regions at a wavelength of 808 nm.

**2.8. In Vivo PTT.** U87MG tumor-bearing mice were randomly divided into four groups ( $n = 5$ ). Two groups of mice were treated with saline and the other two groups treated with PEG-GMF-PPy NPs via intravenous injection. At 24 h postinjection, an 808 nm NIR laser (0.8 W cm<sup>-2</sup>) was applied in one saline-treated group and one PEG-GMF-PPy NP-treated group. Tumor size and body weight of the mice were monitored every 2 days. At 2 h postirradiation, the tumors of different groups were collected and fixed with Z-Fix solution. Then, hematoxylin and eosin (H&E) staining was performed by BBC Biochemical.

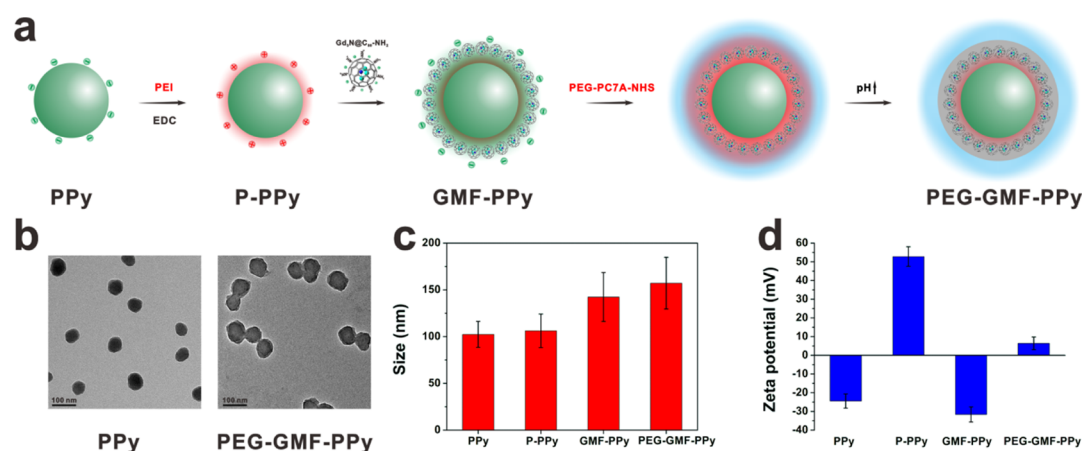


**Figure 2.** Preparation procedure of PEG-GMF-PPy NPs (a). TEM images (b), particle size change (c), and zeta potential change (d) of PEG-GMF-PPy NPs at different fabrication stages.

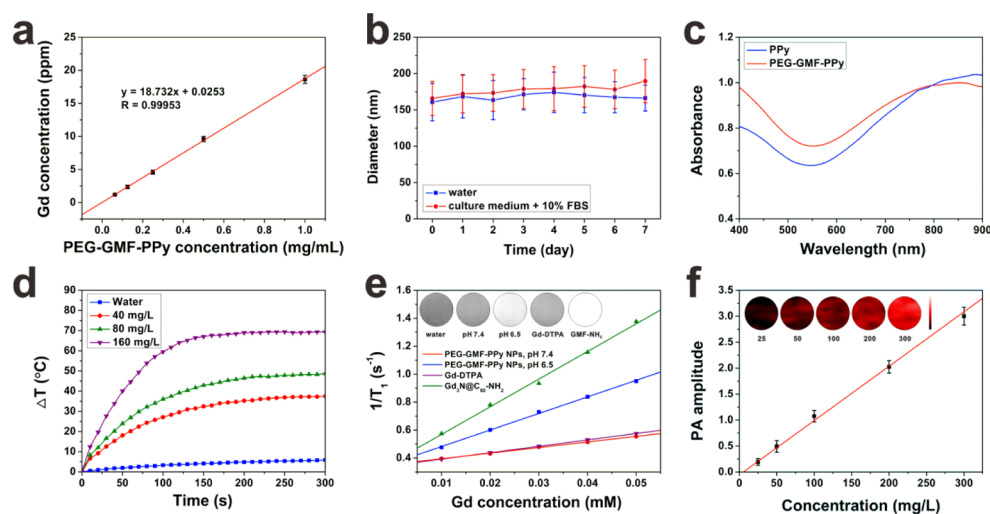


**Figure 3.** (a) Gd concentration (ppm) as a function of the concentration of PEG-GMF-PPy NPs. (b) Colloidal stability of PEG-GMF-PPy NPs in water or culture medium + 10% fetal bovine serum. (c) Absorption spectra of the PPy NPs and PEG-GMF-PPy NPs aqueous solution. (d) Photothermal heating curves of PEG-GMF-PPy NPs solution upon laser irradiation. (e) Longitudinal relaxation rates of PEG-GMF-PPy NPs at different pH conditions. Inset:  $T_1$ -weighted images of different samples. (f) PA signals of the aqueous solution containing PEG-GMF-PPy NPs as a function of concentration. Inset: PA images of PEG-GMF-PPy NPs aqueous solution at different concentrations.

**2.9. Histology Studies.** Mice injected with saline and PEG-GMF-PPy NPs were sacrificed at 30 d postinjection. The major organs of mice were collected and fixed with Z-Fix solution for H&E staining (performed by BBC Biochemical).

### 3. RESULTS AND DISCUSSION

**3.1. Preparation and Characterization of PEG-GMF-PPy NPs.** The chemical structures of PEG-RAFT, C7A monomer, and PEG-PC7A-NHS were analyzed by nuclear magnetic resonance (NMR) and Fourier transform infrared spectroscopy (Figures S1–S5) to confirm successful synthesis. The polymer is suitable for development of tumor pH-responsive systems because the PC7A chains can realize hydrophobic to hydrophilic transition with a transition pH ( $pH_t$ ) of about 6.9.<sup>20</sup> Then, carboxyl-functionalized PPy NPs were prepared by chemical oxidative polymerization of pyrrole and pyrrole-3-carboxylic acid.<sup>46</sup> The diameter of obtained PPy NPs was around 60 nm (Figure 2b). The PPy NPs (Figure S6) showed strong absorbance in the NIR region, and the absorbance at 808 nm was linearly correlated with their concentration (Figure S7). Then, the photothermal effect of

PPy NPs was evaluated in aqueous solution. Upon NIR laser irradiation, the temperature of the PPy NPs solution increased rapidly with a temperature change ( $\Delta T$ ) of 45 °C in 300 s (Figures S8 and S9). The calculated  $\eta$  value of the PPy NPs was 46.2%, which demonstrated great photothermal effect of the PPy NPs. Furthermore, in five laser on–off cycles, the solution temperature still been raised without deterioration, suggesting good photothermal stability of the PPy NPs (Figure S10). All of these results demonstrated that the PPy NP is a great agent and can be used for PTT. One kind of GMF,  $Gd_3N@C_{80}$ , was functionalized by amino groups and hydroxyl groups to form water-soluble  $Gd_3N@C_{80}-NH_2$ .<sup>27,28</sup> The as-prepared functionalized  $Gd_3N@C_{80}-NH_2$  can be well dispersed in water and showed a negative surface charge (Figures S11 and S12).

PEG-GMF-PPy NPs were prepared by a layer-by-layer method. At first, negatively charged PPy NPs were modified by cationic PEI through electrostatic interaction, resulting in positive charged P-PPy NPs. Then, negatively charged  $Gd_3N@C_{80}-NH_2$  was absorbed on the surface of P-PPy NPs through electrostatic interaction. Finally, PEG-PC7A-NHS was con-

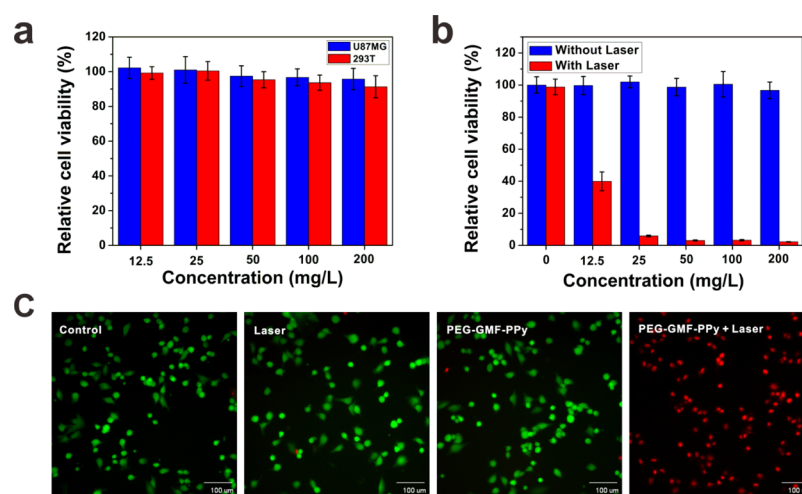


**Figure 4.** (a) Cytotoxicity of PEG-GMF-PPy NPs at different concentrations. (b) Relative viabilities of U87MG cells treated with PEG-GMF-PPy NPs with or without 808 nm laser irradiation. (c) Fluorescence images of co-stained U87MG cells after different treatments. Living cells were stained by calcein AM (green), whereas dead cells were stained by PI (red).

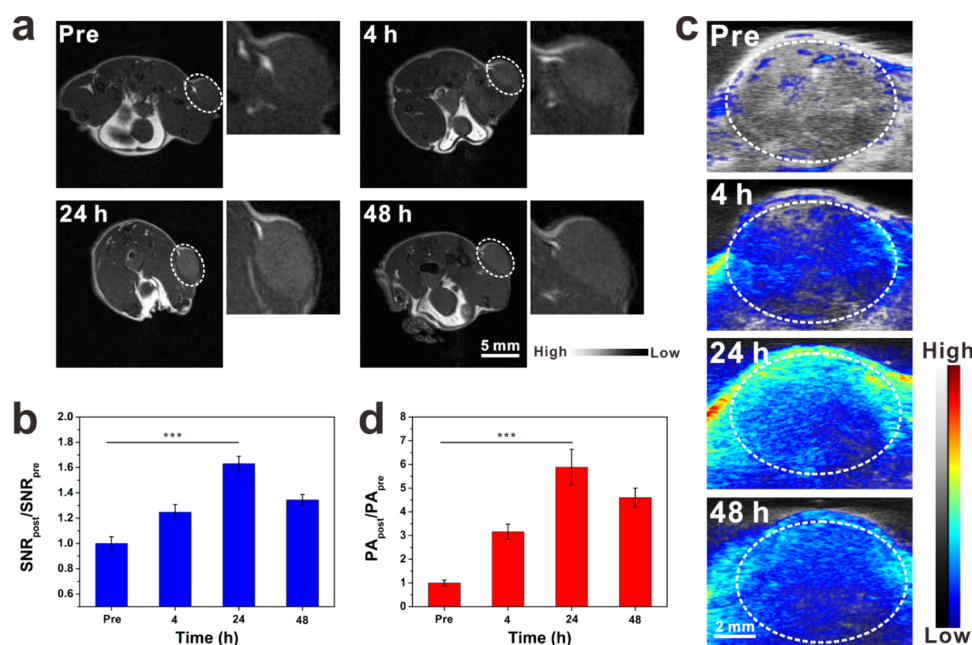


**Figure 5.** (a) In vivo MR images of U87MG tumor-bearing mice after intravenous injection of the PEG-GMF-PPy NPs. (b) SNR changes calculated from the MR images at different time points. (c) In vivo tumor PA images of mice injected with PEG-GMF-PPy NPs. (d) Intensity changes of tumor PA signal. \*\*\* $p < 0.001$ .

jugated to the GMF-PPy NPs by the NHS/NH<sub>2</sub> coupling reaction, obtaining PEG-GMF-PPy NPs (Figure 2a). With more layers of coatings, the size of NPs gradually enlarged (Figure 2b,c). Moreover, after PEI and GMF modification, the zeta potential of the NPs changed from negative to positive and then back to negative; after PEGylation, the PEG-GMF-PPy NPs showed a zeta potential of +6.4 mV (Figure 2d). The diameter and zeta potential changes of the NPs indicated the formation of the PEG-GMF-PPy NPs.

**3.2. Property of PEG-GMF-PPy NPs.** By using ICP-MS, the concentration of Gd in PEG-GMF-PPy NPs solution was determined, which further demonstrated successful formation of PEG-GMF-PPy NPs (Figure 3a). Because of the PEGylation, the PEG-GMF-PPy NPs exhibited good stability (Figure 3b), allowing those nanoparticles for bioapplications. The photothermal property of the PEG-GMF-PPy NPs was

then evaluated in vitro. As shown in Figure 3c, compared to PPy NPs, the PEG-GMF-PPy NPs maintained high NIR absorption. Upon NIR laser irradiation (1.0 W cm<sup>-2</sup>), the  $\Delta T$  of PEG-GMF-PPy NPs solution (40 mg L<sup>-1</sup>) was 37.5 °C in 300 s, demonstrating great photothermal effect of the PEG-GMF-PPy NPs (Figure 3d). To investigate the activated MR imaging, the longitudinal relaxivity ( $r_1$ ) of the PEG-GMF-PPy NPs aqueous solution at different pH values was measured. As shown in Figure 3e, the Gd<sub>3</sub>N@C<sub>80</sub>-NH<sub>2</sub> showed a high  $r_1$  value of 19.79 mM<sup>-1</sup> s<sup>-1</sup>, demonstrating its great MRI performance. The PEG-GMF-PPy NPs showed relatively low MRI contrast capability with an  $r_1$  value of 3.99 mM<sup>-1</sup> s<sup>-1</sup> at pH 7.4, which was similar to that of Gd-DTPA (4.58 mM<sup>-1</sup> s<sup>-1</sup>); however, at pH 6.6, the PEG-GMF-PPy NPs showed a remarkably increased  $r_1$  value of 11.86 mM<sup>-1</sup> s<sup>-1</sup>, which is about 3-fold higher than that examined at pH 7.4 (Figure 3e).

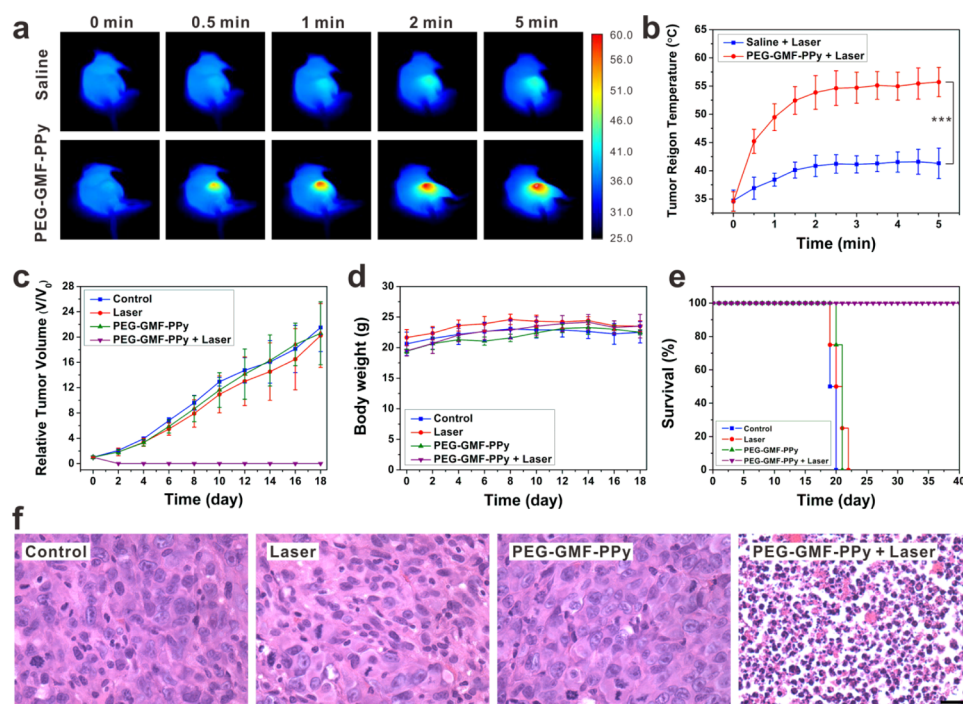


**Figure 6.** (a) Thermal images of mice irradiated with NIR laser at 24 h postinjection of saline or PEG-GMF-PPy NPs. (b) Temperature changes of the tumor regions during laser irradiation. \*\*\* $P < 0.001$ . (c) Tumor growth curves, (d) body weight changes, and (e) survival rate curves of different groups. (f) H&E staining images of tumor sections after laser irradiation. Scale bar is 20  $\mu\text{m}$ .

This pH-activated contrast amplification could be explained by acid-triggered protonation of the coating polymer chains and access of water molecules to the GMF layer. Because of the acidic microenvironment of tumor, the PEG-GMF-PPy NPs can realize tumor-specific MR imaging. We further investigated the PA performance of the PEG-GMF-PPy NPs in vitro. The PEG-GMF-PPy NPs in aqueous solution showed a good PA imaging capability, and the intensities of PA signal at 808 nm were linearly correlated with their concentrations (Figure 3f).

**3.3. Cytotoxicity Study and in Vitro PTT.** Then, the cytotoxicity of the PEG-GMF-PPy NPs was studied in vitro on 293T cells and U87MG cells. Cells were incubated with PEG-GMF-PPy NPs for 24 h, and then, the cell viabilities were measured by the MTT assay. As shown in Figure 4a, the PEG-GMF-PPy NPs did not show obvious toxicity to both 293T cells and U87MG cells. Next, we used PEG-GMF-PPy NPs as the photothermal agent for in vitro tumor cell ablation. U87MG cells incubated with the PEG-GMF-PPy NPs without laser irradiation did not show decreased viability (Figure 4b). In contrast, upon 5 min of laser irradiation ( $1 \text{ W cm}^{-2}$ ), increasing the PEG-GMF-PPy NP concentration resulted in lower tumor cell viability. When incubated with  $25 \text{ mg L}^{-1}$  of PEG-GMF-PPy NPs, more than 90% of cell death was caused by the PTT effect. The in vitro PTT effect was also proved by the live/dead cell staining results. Both the laser-only and PEG-GMF-PPy NP-only groups showed almost no cell death. In contrast, significant cell death was caused by the treatment of PEG-GMF-PPy NPs with laser irradiation (Figure 4c). These results confirmed effective laser-induced photothermal ablation of tumor cells.

**3.4. In Vivo MRI and PAI.** Then, U87MG tumor-bearing mice were used to perform  $T_1$ -weighted MRI in vivo. Before injection of the PEG-GMF-PPy NPs, a relatively low MR signal was observed in the tumor area. However, after intravenous injection of the PEG-GMF-PPy NPs, increased

intensities of tumor MR signal were observed (Figure 5a). The signal-to-noise ratios (SNRs) before and after injection were calculated for quantitative analysis of tumor signal. At 24 h postinjection, the tumor  $T_1$  signal intensity increased by 1.63-fold when compared to preinjection (Figure 5b), which should be attributed to the tumor accumulation and further MR signal activation of the PEG-GMF-PPy NPs. In vivo PA imaging was subsequently carried out. As shown in Figure 5c, PA images were acquired at preinjection and 4, 24, and 48 h postinjection. The intensities of PA signal in the tumor region gradually increased until 24 h, showing 5.88-fold increase at 24 h postinjection when compared with the PA signal pre-injection (Figure 5c,d), indicating capability of the PEG-GMF-PPy NPs for PA imaging. These in vivo imaging results suggest that the PEG-GMF-PPy NP is a great agent for tumor dual-modal imaging.

**3.5. In Vivo PTT.** To perform the in vivo PTT treatment, saline or PEG-GMF-PPy NPs were intravenously injected into U87MG tumor-bearing mice. At 24 h postinjection, a 5 min of 808 nm NIR laser irradiation ( $0.8 \text{ W cm}^{-2}$ ) was applied on tumor areas. As shown in Figure 6a,b, for the mice injected with the PEG-GMF-PPy NPs, the temperature of tumor region rapidly increased during laser irradiation and reached to about  $55^\circ\text{C}$  in 2 min. However, for the saline-treated mice, the temperature of the tumor region showed a slight increase ( $\sim 5^\circ\text{C}$ ). These results confirmed great photothermal effect of the PEG-GMF-PPy NPs in vivo. After laser irradiation, one mouse in each group was euthanized and the tumors were harvested for H&E staining to determine the PTT effect. As shown in Figure 6f, for the PEG-GMF-PPy NP-and laser irradiation-treated group, the tumors showed obvious cell damage, which was attributed to the hyperthermia induced by the photothermal effect. As a result, the tumors were completely eradicated without recurrence in the PTT group (Figures 6c and S13). Furthermore, the survival of the mice with PTT

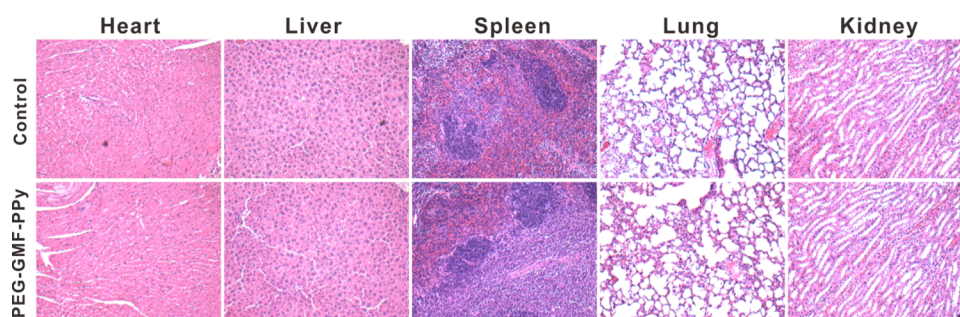


Figure 7. H&E staining of major organs. Scale bar is 200  $\mu\text{m}$ .

treatment was greatly prolonged (Figure 6e). In contrast, the PEG-GMF-PPy group and laser-only group showed negligible antitumor effect. During the experiment, no noticeable body weight loss was observed in all of the four groups, indicating no systemic toxicity (Figure 6d). The H&E staining of major organs collected at 30 d postinjection demonstrated that no noticeable organ damage was caused by PEG-GMF-PPy NPs (Figure 7).

#### 4. CONCLUSIONS

In summary, a theranostic agent (PEG-GMF-PPy NPs) was developed for activatable MR/PA dual-modal imaging-guided PTT. Through layer-by-layer modification, a potential next-generation MR contrast agent (GMF) and an ultra-pH-responsive polymer (PEG-PC7A) were successively modified to the surface of photothermal agent (PPy NP). The obtained PEG-GMF-PPy NPs showed strong NIR absorption, good biocompatibility, and stability. At tumor extracellular pH, the PEG-GMF-PPy NPs can achieve pH-activated MR and effective PA dual-modal imaging to guide PTT. In vivo cancer treatment showed efficient tumor ablation upon NIR laser irradiation. The in vitro and in vivo results suggest that the PEG-GMF-PPy NPs is a promising theranostic agent for accurate diagnosis-guided cancer PTT.

#### ■ ASSOCIATED CONTENT

##### Supporting Information

The Supporting Information is available free of charge on the ACS Publications website at DOI: 10.1021/acsami.8b09670.

Synthesis process and NMR characterization of the monomer and polymer; characterizations of PPy NPs and  $\text{Gd}_3\text{N}@C_{80}\text{-NH}_2$ ; and photographs of U87MG tumor-bearing mice after PTT treatment (PDF)

#### ■ AUTHOR INFORMATION

##### Corresponding Authors

\*E-mail: wangjing@fmmu.edu.cn (J.W.).

\*E-mail: shawn.chen@nih.gov (X.C.).

##### ORCID

Yunlu Dai: 0000-0003-4023-7320

Xiaoyuan Chen: 0000-0002-9622-0870

##### Notes

The authors declare no competing financial interest.

#### ■ ACKNOWLEDGMENTS

This work was supported by the Shaanxi Science & Technology Coordination & Innovation Project (2016KTCQ03-09), The International Cooperation Program

of Xijing Hospital (XJZT15G01), Shaanxi Innovation Capability Support Plan (2018PT-08), and the Intramural Research Program (IRP) of the National Institute of Biomedical Imaging and Bioengineering (NIBIB), National Institutes of Health (NIH).

#### ■ REFERENCES

- (1) Cheng, L.; Wang, C.; Feng, L.; Yang, K.; Liu, Z. Functional Nanomaterials for Phototherapies of Cancer. *Chem. Rev.* **2014**, *114*, 10869–10939.
- (2) Wang, Y.; Yang, T.; Ke, H.; Zhu, A.; Wang, Y.; Wang, J.; Shen, J.; Liu, G.; Chen, C.; Zhao, Y.; Chen, H. Smart Albumin-Biomaterialized Nanocomposites for Multimodal Imaging and Photothermal Tumor Ablation. *Adv. Mater.* **2015**, *27*, 3874–3882.
- (3) Meng, Z.; Wei, F.; Wang, R.; Xia, M.; Chen, Z.; Wang, H.; Zhu, M. NIR-Laser-Switched *In Vivo* Smart Nanocapsules for Synergistic Photothermal and Chemotherapy of Tumors. *Adv. Mater.* **2016**, *28*, 245–253.
- (4) Wang, Z.; Huang, P.; Jacobson, O.; Wang, Z.; Liu, Y.; Lin, L.; Lin, J.; Lu, N.; Zhang, H.; Tian, R.; Niu, G.; Liu, G.; Chen, X. Biomaterialization-Inspired Synthesis of Copper Sulfide-Ferritin Nanocages as Cancer Theranostics. *ACS Nano* **2016**, *10*, 3453–3460.
- (5) Zhang, L.; Chen, Y.; Li, Z.; Li, L.; Saint-Cricq, P.; Li, C.; Lin, J.; Wang, C.; Su, Z.; Zink, J. I. Tailored Synthesis of Octopus-Type Janus Nanoparticles for Synergistic Actively-Targeted and Chemo-Photothermal Therapy. *Angew. Chem., Int. Ed.* **2016**, *55*, 2118–2121.
- (6) Ai, X.; Mu, J.; Xing, B. Recent Advances of Light-Mediated Theranostics. *Theranostics* **2016**, *6*, 2439–2457.
- (7) Lin, J.; Wang, M.; Hu, H.; Yang, X.; Wen, B.; Wang, Z.; Jacobson, O.; Song, J.; Zhang, G.; Niu, G.; Huang, P.; Chen, X. Multimodal-Imaging-Guided Cancer Phototherapy by Versatile Biomimetic Theranostics with UV and  $\gamma$ -Irradiation Protection. *Adv. Mater.* **2016**, *28*, 3273–3279.
- (8) Deng, L.; Cai, X.; Sheng, D.; Yang, Y.; Strohm, E. M.; Wang, Z.; Ran, H.; Wang, D.; Zheng, Y.; Li, P.; Shang, T.; Ling, Y.; Wang, F.; Sun, Y. A Laser-Activated Biocompatible Theranostic Nanoagent for Targeted Multimodal Imaging and Photothermal Therapy. *Theranostics* **2017**, *7*, 4410–4423.
- (9) Lyu, Y.; Cui, D.; Sun, H.; Miao, Y.; Duan, H.; Pu, K. Dendronized Semiconducting Polymer as Photothermal Nanocarrier for Remote Activation of Gene Expression. *Angew. Chem., Int. Ed.* **2017**, *129*, 9283–9287.
- (10) Deng, X.; Li, K.; Cai, X.; Liu, B.; Wei, Y.; Deng, K.; Xie, Z.; Wu, Z.; Ma, P.; Hou, Z.; Cheng, Z.; Lin, J. A Hollow-Structured  $\text{Cu}_2\text{S}@Au$  Nanohybrid: Synergistically Enhanced Photothermal Efficiency and Photoswitchable Targeting Effect for Cancer Theranostics. *Adv. Mater.* **2017**, *29*, 1701266.
- (11) Lin, L.-S.; Yang, X.; Zhou, Z.; Yang, Z.; Jacobson, O.; Liu, Y.; Yang, A.; Niu, G.; Song, J.; Yang, H.-H.; Chen, X. Yolk-Shell Nanostructure: An Ideal Architecture to Achieve Harmonious Integration of Magnetic-Plasmonic Hybrid Theranostic Platform. *Adv. Mater.* **2017**, *29*, 1606681.
- (12) Ge, J.; Jia, Q.; Liu, W.; Guo, L.; Liu, Q.; Lan, M.; Zhang, H.; Meng, X.; Wang, P. Red-Emissive Carbon Dots for Fluorescent,

Photoacoustic, and Thermal Theranostics in Living Mice. *Adv. Mater.* **2015**, *27*, 4169–4177.

(13) Wang, S.; Lin, J.; Huang, P. Advances on the Use of Biodegradable Proteins/Peptides in Photothermal Theranostics. *J. Nanomater.* **2016**, *2016*, 5810952.

(14) Zhu, H.; Fang, Y.; Miao, Q.; Qi, X.; Ding, D.; Chen, P.; Pu, K. Regulating Near-Infrared Photodynamic Properties of Semiconducting Polymer Nanotheranostics for Optimized Cancer Therapy. *ACS Nano* **2017**, *11*, 8998–9009.

(15) Yang, W.; Guo, W.; Le, W.; Lv, G.; Zhang, F.; Shi, L.; Wang, X.; Wang, J.; Wang, S.; Chang, J.; Zhang, B. Albumin-Bioinspired Gd:CuS Nanotheranostic Agent for *In Vivo* Photoacoustic/Magnetic Resonance Imaging-Guided Tumor-Targeted Photothermal Therapy. *ACS Nano* **2016**, *10*, 10245–10257.

(16) Lv, G.; Guo, W.; Zhang, W.; Zhang, T.; Li, S.; Chen, S.; Eltahan, A. S.; Wang, D.; Wang, Y.; Zhang, J.; Wang, P. C.; Chang, J.; Liang, X.-J. Near-Infrared Emission CuInS/ZnS Quantum Dots: All-in-One Theranostic Nanomedicines with Intrinsic Fluorescence/Photoacoustic Imaging for Tumor Phototherapy. *ACS Nano* **2016**, *10*, 9637–9645.

(17) Ke, K.; Yang, W.; Xie, X.; Liu, R.; Wang, L.-L.; Lin, W.-W.; Huang, G.; Lu, C.-H.; Yang, H.-H. Copper Manganese Sulfide Nanoplates: A New Two-Dimensional Theranostic Nanoplateform for MRI/MSOT Dual-Modal Imaging-Guided Photothermal Therapy in the Second Near-Infrared Window. *Theranostics* **2017**, *7*, 4763–4776.

(18) Li, D.; Zhang, G.; Xu, W.; Wang, J.; Wang, Y.; Qiu, L.; Ding, J.; Yang, X. Investigating the Effect of Chemical Structure of Semiconducting Polymer Nanoparticle on Photothermal Therapy and Photoacoustic Imaging. *Theranostics* **2017**, *7*, 4029–4040.

(19) Ding, B.; Yu, C.; Li, C.; Deng, X.; Ding, J.; Cheng, Z.; Xing, B.; Ma, P.; Lin, J. cis-Platinum Pro-Drug-Attached CuFeS<sub>2</sub> Nanoplates for *In Vivo* Photothermal/Photoacoustic Imaging and Chemotherapy/Photothermal Therapy of Cancer. *Nanoscale* **2017**, *9*, 16937–16949.

(20) Wang, Y.; Zhou, K.; Huang, G.; Hensley, C.; Huang, X.; Ma, X.; Zhao, T.; Sumer, B. D.; DeBerardinis, R. J.; Gao, J. A Nanoparticle-Based Strategy for the Imaging of a Broad Range of Tumours by Nonlinear Amplification of Microenvironment Signals. *Nat. Mater.* **2014**, *13*, 204–212.

(21) Zheng, X.; Mao, H.; Huo, D.; Wu, W.; Liu, B.; Jiang, X. Successively Activatable Ultrasensitive Probe for Imaging Tumour Acidity and Hypoxia. *Nat. Biomed. Eng.* **2017**, *1*, 0057.

(22) Hu, X.; Liu, G.; Li, Y.; Wang, X.; Liu, S. Cell-Penetrating Hyperbranched Polyprodrug Amphiphiles for Synergistic Reductive Milieu-Triggered Drug Release and Enhanced Magnetic Resonance Signals. *J. Am. Chem. Soc.* **2015**, *137*, 362–368.

(23) Viger, M. L.; Sankaranarayanan, J.; de Gracia Lux, C.; Chan, M.; Almutairi, A. Collective Activation of MRI Agents Via Encapsulation and Disease-Triggered Release. *J. Am. Chem. Soc.* **2013**, *135*, 7847–7850.

(24) Mi, P.; Kokuryo, D.; Cabral, H.; Wu, H.; Terada, Y.; Saga, T.; Aoki, I.; Nishiyama, N.; Kataoka, K. A pH-Activatable Nanoparticle with Signal-Amplification Capabilities for Non-Invasive Imaging of Tumour Malignancy. *Nat. Nanotechnol.* **2016**, *11*, 724–730.

(25) Mikawa, M.; Kato, H.; Okumura, M.; Narazaki, M.; Kanazawa, Y.; Miwa, N.; Shinohara, H. Paramagnetic Water-Soluble Metallofullerenes Having the Highest Relaxivity for MRI Contrast Agents. *Bioconjugate Chem.* **2001**, *12*, 510–514.

(26) Chen, Z.; Ma, L.; Liu, Y.; Chen, C. Applications of Functionalized Fullerenes in Tumor Theranostics. *Theranostics* **2012**, *2*, 238–250.

(27) Li, T.; Murphy, S.; Kiselev, B.; Bakshi, K. S.; Zhang, J.; Eltahir, A.; Zhang, Y.; Chen, Y.; Zhu, J.; Davis, R. M.; Madsen, L. A.; Morris, J. R.; Karolyi, D. R.; LaConte, S. M.; Sheng, Z.; Dorn, H. C. A New Interleukin-13 Amino-Coated Gadolinium Metallofullerene Nanoparticle for Targeted MRI Detection of Glioblastoma Tumor Cells. *J. Am. Chem. Soc.* **2015**, *137*, 7881–7888.

(28) Zheng, J.-p.; Zhen, M.-M.; Ge, J.-C.; Liu, Q.-L.; Jiang, F.; Shu, C.-Y.; Alhadlaq, H. A.; Wang, C.-R. Multifunctional Gadofulleride Nanoprobe for Magnetic Resonance Imaging/Fluorescent Dual

Modality Molecular Imaging and Free Radical Scavenging. *Carbon* **2013**, *65*, 175–180.

(29) Li, T.; Dorn, H. C. Biomedical Applications of Metal-Encapsulated Fullerene Nanoparticles. *Small* **2017**, *13*, 1603152.

(30) Adisheshaiah, P.; Dellinger, A.; MacFarland, D.; Stern, S.; Dobrovolskaia, M.; Ileva, L.; Patri, A. K.; Bernardo, M.; Brooks, D. B.; Zhou, Z.; McNeil, S.; Kepley, C. A Novel Gadolinium-Based Trimetaspere Metallofullerene for Application as a Magnetic Resonance Imaging Contrast Agent. *Invest. Radiol.* **2013**, *48*, 745–754.

(31) Guo, W.; Sun, X.; Jacobson, O.; Yan, X.; Min, K.; Srivatsan, A.; Niu, G.; Kiesewetter, D. O.; Chang, J.; Chen, X. Intrinsically Radioactive [<sup>64</sup>Cu]CuInS/ZnS Quantum Dots for PET and Optical Imaging: Improved Radiochemical Stability and Controllable Ceramkov Luminescence. *ACS Nano* **2015**, *9*, 488–495.

(32) Liu, Y.; Kang, N.; Lv, J.; Zhou, Z.; Zhao, Q.; Ma, L.; Chen, Z.; Ren, L.; Nie, L. Deep Photoacoustic/Luminescence/Magnetic Resonance Multimodal Imaging in Living Subjects Using High-Efficiency Upconversion Nanocomposites. *Adv. Mater.* **2016**, *28*, 6411–6419.

(33) Wang, S.; Lin, J.; Wang, Z.; Zhou, Z.; Bai, R.; Lu, N.; Liu, Y.; Fu, X.; Jacobson, O.; Fan, W.; Qu, J.; Chen, S.; Wang, T.; Huang, P.; Chen, X. Core-Satellite Polydopamine-Gadolinium-Metallofullerene Nanotheranostics for Multimodal Imaging Guided Combination Cancer Therapy. *Adv. Mater.* **2017**, *29*, 1701013.

(34) Zhou, Z.; Huang, D.; Bao, J.; Chen, Q.; Liu, G.; Chen, Z.; Chen, X.; Gao, J. A Synergistically Enhanced T<sub>1</sub>-T<sub>2</sub> Dual-Modal Contrast Agent. *Adv. Mater.* **2012**, *24*, 6223–6228.

(35) Li, L.; Jiang, W.; Luo, K.; Song, H.; Lan, F.; Wu, Y.; Gu, Z. Superparamagnetic Iron Oxide Nanoparticles as MRI Contrast Agents for Non-Invasive Stem Cell Labeling and Tracking. *Theranostics* **2013**, *3*, 595–615.

(36) Ni, D.; Bu, W.; Ehlerding, E. B.; Cai, W.; Shi, J. Engineering of Inorganic Nanoparticles as Magnetic Resonance Imaging Contrast Agents. *Chem. Soc. Rev.* **2017**, *46*, 7438–7468.

(37) Lin, J.; Chen, X.; Huang, P. Graphene-Based Nanomaterials for Bioimaging. *Adv. Drug Delivery Rev.* **2016**, *105*, 242–254.

(38) Shakiba, M.; Ng, K. K.; Huynh, E.; Chan, H.; Charron, D. M.; Chen, J.; Muhanna, N.; Foster, F. S.; Wilson, B. C.; Zheng, G. Stable J-Aggregation Enabled Dual Photoacoustic and Fluorescence Nanoparticles for Intraoperative Cancer Imaging. *Nanoscale* **2016**, *8*, 12618–12625.

(39) Wang, S.; Lin, J.; Wang, T.; Chen, X.; Huang, P. Recent Advances in Photoacoustic Imaging for Deep-Tissue Biomedical Applications. *Theranostics* **2016**, *6*, 2394–2413.

(40) Liu, Y.; Wang, S.; Ma, Y.; Lin, J.; Wang, H.-Y.; Gu, Y.; Chen, X.; Huang, P. Ratiometric Photoacoustic Molecular Imaging for Methylmercury Detection in Living Subjects. *Adv. Mater.* **2017**, *29*, 1606129.

(41) Nie, L.; Chen, X. Structural and Functional Photoacoustic Molecular Tomography Aided by Emerging Contrast Agents. *Chem. Soc. Rev.* **2014**, *43*, 7132–7170.

(42) Guo, B.; Sheng, Z.; Kenry, K.; Hu, D.; Lin, X.; Xu, S.; Liu, C.; Zheng, H.; Liu, B. Biocompatible Conjugated Polymer Nanoparticles for Highly Efficient Photoacoustic Imaging of Orthotopic Brain Tumors in the Second Near-Infrared Window. *Mater. Horiz.* **2017**, *4*, 1151–1156.

(43) Xie, C.; Zhen, X.; Lei, Q.; Ni, R.; Pu, K. Self-Assembly of Semiconducting Polymer Amphiphiles for *In Vivo* Photoacoustic Imaging. *Adv. Funct. Mater.* **2017**, *27*, 1605397.

(44) Zhou, K.; Wang, Y.; Huang, X.; Luby-Phelps, K.; Sumer, B. D.; Gao, J. Tunable, Ultrasensitive pH-Responsive Nanoparticles Targeting Specific Endocytic Organelles in Living Cells. *Angew. Chem., Int. Ed.* **2011**, *50*, 6109–6114.

(45) Kim, S.; Oh, W.-K.; Jeong, Y. S.; Hong, J.-Y.; Cho, B.-R.; Hahn, J.-S.; Jang, J. Cytotoxicity of, and Innate Immune Response to, Size-Controlled Polypyrrole Nanoparticles in Mammalian Cells. *Biomaterials* **2011**, *32*, 2342–2350.

(46) Liang, X.; Li, Y.; Li, X.; Jing, L.; Deng, Z.; Yue, X.; Li, C.; Dai, Z. PEGylated Polypyrrole Nanoparticles Conjugating Gadolinium Chelates for Dual-Modal MRI/Photoacoustic Imaging Guided Photothermal Therapy of Cancer. *Adv. Funct. Mater.* **2015**, *25*, 1451–1462.